

REVIEW ARTICLE OPEN



Effects of the microstructure and retained/reversed austenite on the corrosion behavior of NiCrMoV/Nb high-strength steel

Chao Hai^{1,2}, Yuetong Zhu^{1,2}, Endian Fan^{1,2}, Cuiwei Du^{1,2}✉, Xuequn Cheng^{1,2} and Xiaogang Li^{1,2}

A comparison of microstructure and corrosion performance has been made between NiCrMoV/Nb steel under different heat treatments in artificial seawater. The microstructures as well as the volume fraction of austenite strongly affect corrosion resistance. Atomic force microscopy (AFM) results reveal that both retained/reversed austenite and the grain boundary have a higher Volta potential than the matrix. The morphology of pits and the nature of retained/reversed austenite were investigated by field emission scanning electron microscopy (FESEM). Results can be discussed in terms of a model that describes the microgalvanic effect and the change of morphology and content of retained/reversed austenite resulting from a heat treatment process. The role of the microstructure and retained austenite on corrosion resistance evolution in the corrosion process is discussed. The X-ray diffraction (XRD) results reveal that the corrosion products formed on distinct microstructures primarily contain lepidocrocite (γ -FeOOH), goethite (α -FeOOH) with little difference after long time immersion.

npj Materials Degradation (2023)7:40; <https://doi.org/10.1038/s41529-023-00361-6>

INTRODUCTION

High carbon content of NiCrMoV/Nb steels causes problems for welding, making steel applications limited in the marine industry. Under this condition, NiCrMoV/Nb steels with low carbon content are developed to overcome those concerns, which these steels exhibit high strength and toughness, together with good low-temperature toughness. Compared with the traditional modulation heat treatment, a mixed microstructure of austenite phase and martensite phase could be achieved by means of quenching-lamellarizing-tempering (QLT)^{1,2} heat treatment^{3,4}, which could obtain good comprehensive properties by adjusting the strength and toughness. Additionally, extensive works^{5,6} have been conducted on the formation mechanism of the revised austenite and focus more attention on the influence of austenite on the mechanical property.

However, in the sea engineering application, corrosion may occur. The microstructure and retained austenite have complex influences on the corrosion resistance. Studies^{7–12} have been undertaken about the effect of microstructure on corrosion resistance of low-alloy steel and stainless steel. Wu et al.¹³ studied the microstructural evolution during aging and its impact on the corrosion behavior and mechanism of the Fe-19Mn-0.8C-5Ni low-density steel. They emphasized that aging improves the corrosion resistance of the steel, which inhibits the microgalvanic effect at the initial stage and alleviates the local acidification at the later stage. Ma et al.¹⁴ examined the potential difference between the M/A island and the bainite component in E690 low-alloy steel using SKPFM. The M/A as the cathode phase can induce the preferential dissolution of the bainite structure at the edge of the M/A island and promote local corrosion. Moreover, the effect of different austempering heat treatments on the corrosion properties of high silicon steel was investigated by Mattia et al.¹⁵ They found that the corrosion resistance of the samples increased with increases in the volume fraction of retained austenite due to lower amounts of residual stresses. Moreover, the author in ref. ¹⁶ analyzed the various effects of nickel addition and austempering

on the microstructure and corrosion resistance of ductile irons. They found that the retained austenite in ductile iron could improve the corrosion resistance owing to its greatest corrosion inhibition efficiency. However, those studies were contradictory and failed to consider the effect of retained austenite on the corrosion behavior. Furthermore, studies on the effect of retained austenite on corrosion resistance have revealed that retained austenite in stainless steel is not the precursor of pits, whereas pits are generally initiated at these locations with chemical or mechanical heterogeneities^{17–19}. However, the transformation of phase and enrichment of Ni and C in the retained austenite could be occurred during heat treatment process. It is predictable that the corrosion behavior of the NiCrMoV/Nb steel will also change with the microstructure and the contents of retained/reversed austenite. The effect of the retained austenite on the corrosion behavior should be further investigated owing to limit research nowadays.

Based on the above considerations, the macroscopical and microscopic characterization of the structure of different heat-treated processes were carried out by SEM, XRD and transmission electron microscopy (TEM). The corrosion behavior of different heat-treated samples was investigated using AFM technology combined with an immersion experiment. Finally, the effect of microstructure and retained austenite on the corrosion evolution of steel was investigated, and the corrosion mechanisms of microstructure and retained/reversed austenite were clarified.

RESULTS

Microstructure characteristics

As is well known, the structure has a significant influence on the corrosion resistance of steel. The SEM and TEM microstructural morphology of the Q, QT and QLT specimens is shown in Fig. 1. The microstructure of the Q specimen mainly consists of lath martensite without a relevant amount of retained austenite. After tempering at 600 °C, the microstructure presents tempered

¹Institute of Advanced Materials and Technology, University of Science and Technology Beijing, 100083 Beijing, China. ²National Materials Corrosion and Protection Data Center, 100083 Beijing, China. ✉email: dcw@ustb.edu.cn

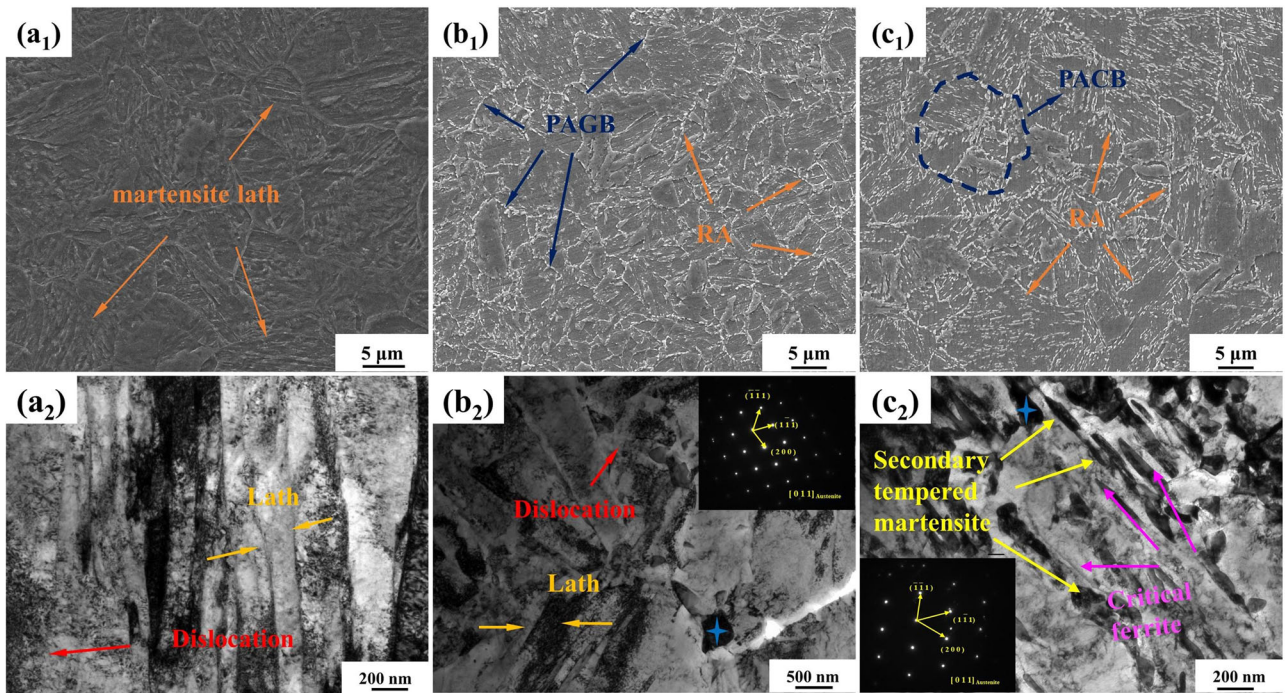


Fig. 1 The microstructure of (a₁–a₂) Q, (b₁–b₂) QT, and (c₁–c₂) QLT samples, where a₁, b₁ and c₁ are SEM micrographs, a₂, b₂, and c₂ are TEM micrographs, respectively.

martensite. White particle-platelets (orange arrow in Fig. 1b) can be observed at the grain boundary or inside the martensite grains (both in lath borders and packet borders), and they are distributed evenly. A two-phase region heat treatment was conducted on the QT sample. It reduces the grain size slightly and makes the microstructure distribution more uniform. Three specimens are characterized in detail by transmission electron microscopy. It can be seen from Fig. 1a₂ that the martensite boundary of the directly quenched steel is relatively obvious. A lot of dislocations were observed in the lath, where local entanglement forms dislocation packages (as shown by the red arrow). The martensite boundary of QT heat-treated steel becomes unobvious due to the migration of some lath boundaries during tempering, and the dislocation density decreases in the steel. Meanwhile, blocky material is observed at the grain boundary. The selected electron diffraction (SED) results show that the material has a face-centered cubic (FCC) structure, which could be the retained austenite (RA). The morphology of QLT steel has changed significantly. A large amount of secondary tempered martensite has been formed in the steel, which is distributed along the original martensite lath borders or packet borders. SED results show that the crystal structure is also FCC, which may be the reversed austenite formed during secondary quenching and subsequent tempering.

The X-ray diffraction pattern for three samples is shown in Fig. 2 and can be compared. According to the XRD results, the Q sample has obvious body-centered cubic (BCC) structure only without retained austenite, while the QT and QLT samples also have obvious austenite phase peaks with differences in strength. The content of retained/reversed austenite for QT and QLT specimens calculated by the Eqs. (6) and (7) was 4.8% and 13.8%, respectively.

Localized corrosion morphology at the early stage

In order to trace the process of pitting initiation induced by different microstructures, immersion experiments are performed on three samples. Figures 3–5 show the FE-SEM images of three specimens after they were immersed for 120 min and removal of rust. After immersion, obvious local corrosion has occurred in all

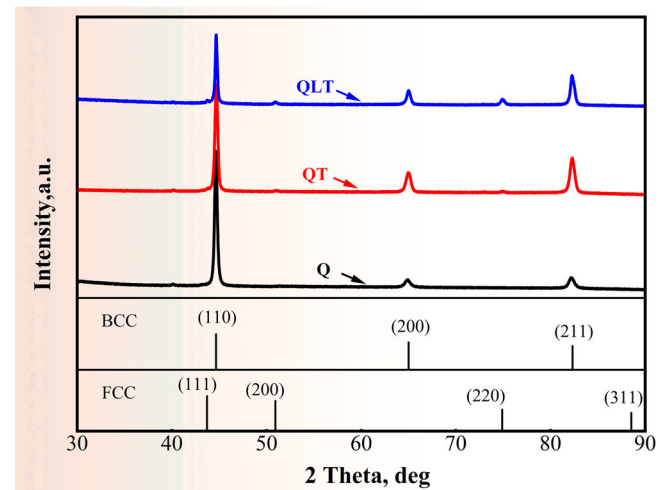


Fig. 2 XRD spectra of samples after different heat treatments.

three specimens, and a significant number of large pits can be observed on the surface of the Q sample (as shown in Fig. 3a). According to the analysis results, the initiation positions of the pits are mostly formed at the lath or grain boundary. In addition, the surrounding areas of inclusion (Fig. 3e, f are the EDS analysis results of inclusion) also could be the initiation sites of pits^{8,20}. For the QT sample, both the number and size of pits are greatly reduced (Fig. 4a). As shown in Fig. 4b, d–f, pits are initiated at the interface of the retained austenite and matrix distributed on the PAGB or inside the martensite grains (both in lath borders and packet borders). In addition, some small pits may also be observed inside the grains, which may form from nanoparticles (VC or NbC) during the corrosion process. Pits for the QLT sample are almost initiated at the interface of the revised austenite and matrix (distributed in PAGB or in lath borders and packet borders) (Fig. 5c, d). Figure 6c shows that the matrix dissolved obviously, and only the revised austenite is retained as a noble area. Both QT

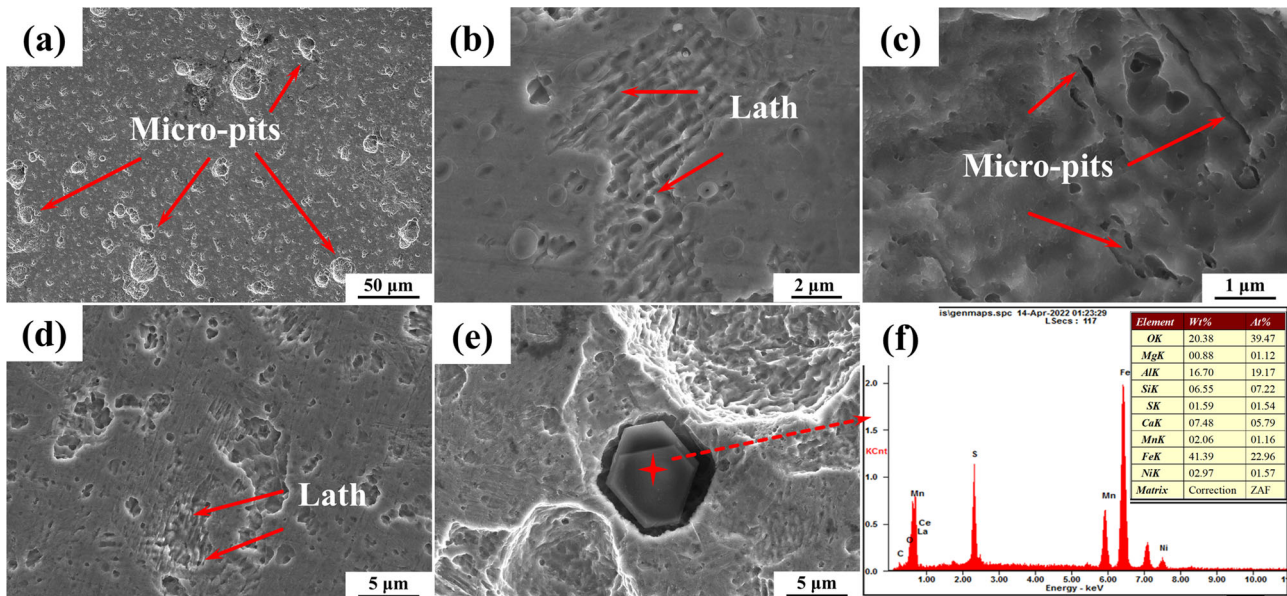


Fig. 3 Corrosion morphology of the micro-pits in Q specimen after 120 min immersion times.

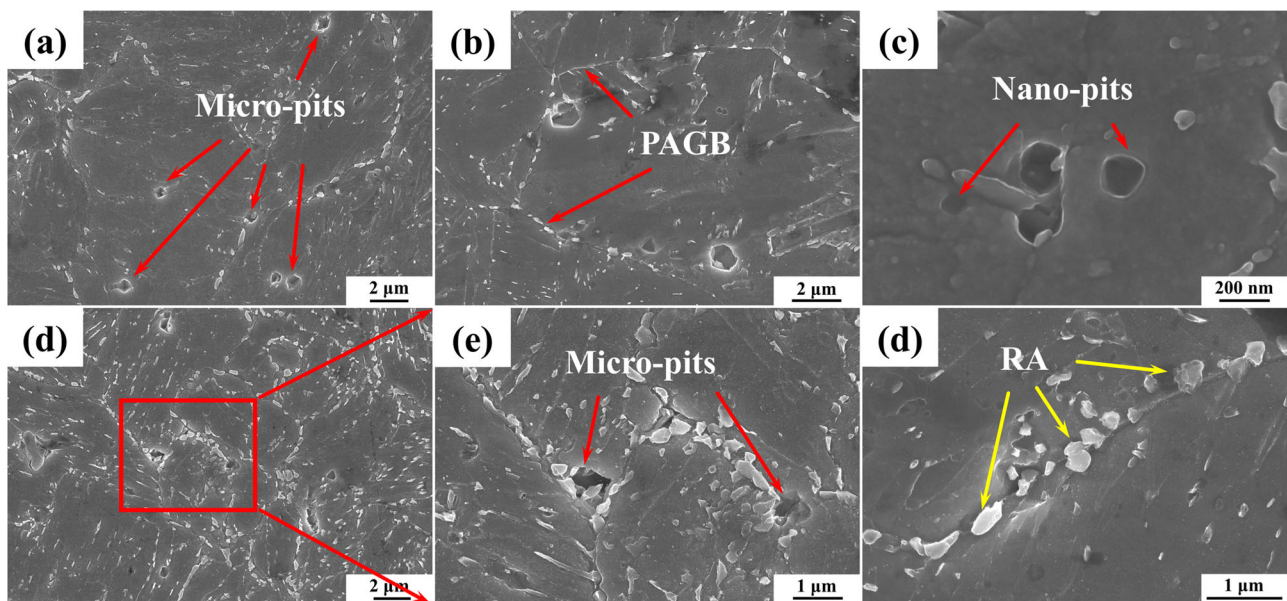


Fig. 4 Corrosion morphology of the micro-pits in QT specimen after 120 min immersion times.

steel and QLT steel show the characteristics of preferential dissolution of the matrix. The different heat treatments lead to significant changes in the nucleation sites and number of pits. It is indicated that the microstructure and reversed austenite have an important influence on the initiation process of pits.

Corrosion rate

The uniform corrosion rates of three samples after different immersion times are shown in Fig. 6. At the initial immersion stage, the corrosion rate of three samples increases with time. After immersion for 60 days, the corrosion rates of the QLT and Q samples decrease rapidly, while the QT sample decreases slightly. Additionally, at the beginning, the corrosion rate is ranked as $QT < Q < QLT$. After immersion for 180 days, the corrosion rate of the QT specimen is also the lowest, and the corrosion rates of the Q and QT samples are not much different, with the corrosion rate

following the order: $QT < Q < QLT$. When comparing the three samples, the initial immersion stage shows a greater difference in corrosion rate, and this trend becomes less pronounced over time.

Corrosion product layer analysis

The cross-sectional morphology of three samples with different immersion times is also analyzed. As shown in Figs. 7–10, the corrosion product layer is a single layer without stratification (cannot distinguish an inner layer and an outer layer), which is relatively loose and contains a lot of cavities and cracks. The thickness of the rust layer in the three samples shows an increasing trend with the immersion time. Compared with the Q sample and QT sample, the thickness of the rust layer on the QLT sample is thicker after immersion for 30 days. The rust layer is relatively loose and contains a lot of holes, which indicates that the protective performance of the rust layer is poor. With the

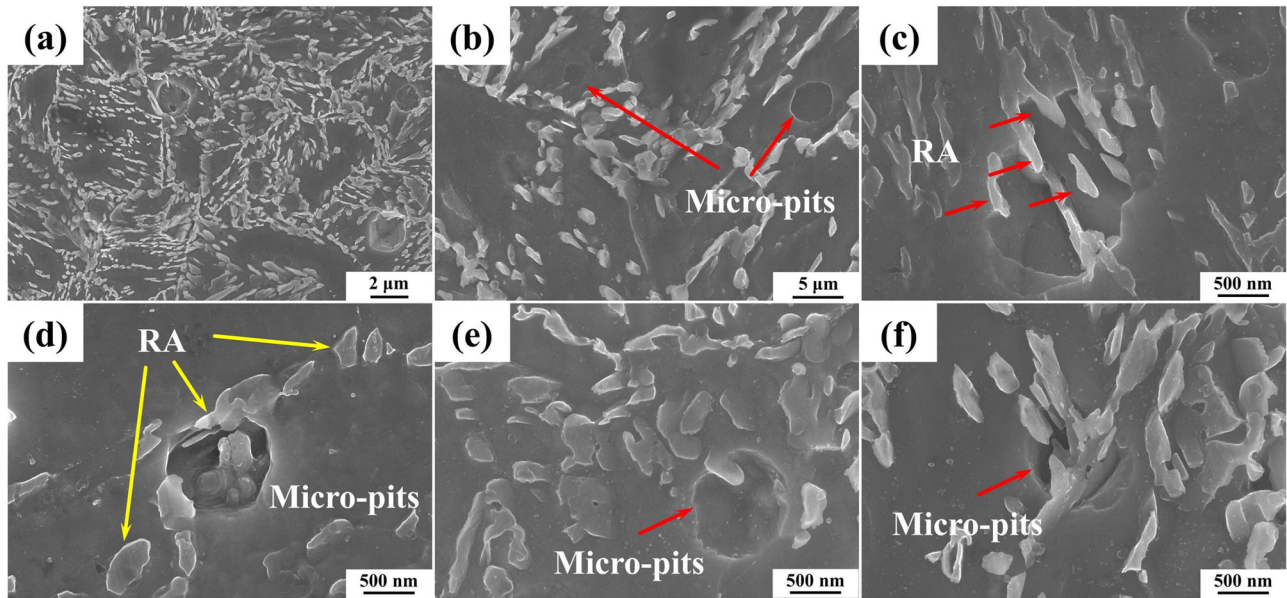


Fig. 5 Corrosion morphology of the micro-pits in QLT specimen after 120 min immersion times.

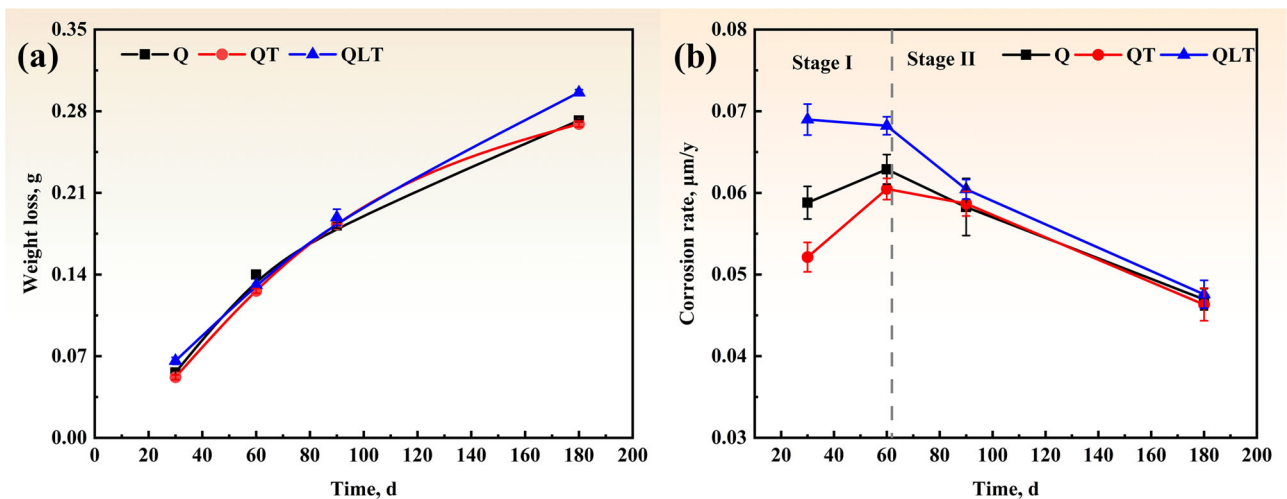


Fig. 6 Weight loss and corrosion rate of three samples for different immersion time periods.

increase in immersion time, the product layer becomes thicker and relatively dense, which can effectively block the transmission of corrosive media and decrease the corrosion of the matrix.

The element distribution shows that Mo, Ni, and O are uniformly distributed throughout the corrosion product layer for three samples after immersion for 30 days, while only Cr and Ca enrich in the rust layer. Little difference in element distribution among the three samples. There is an enrichment of Ni and Mo in the corrosion product with the increase in immersion time, as shown in Figs. 7–10. Cl is mainly distributed throughout the corrosion product layer in three samples, indicating that this layer does not hinder the entry of corrosive ions. After immersion for 180 days, Cl is enriched outside the rust layer, indicating that the product layer has certain protection and can inhibit the diffusion of Cl. In general, the different corrosion processes in the three samples are responsible for these differences.

The composition analysis of corrosion product layer

Figure 11 shows the phase composition of corrosion product layers in three samples. The phase compositions of the three

samples are consistent; they are composed of α -FeOOH and γ -FeOOH without a Fe_3O_4 component. The corrosion is the slightest, and the transformation to Fe_3O_4 has not yet occurred under full immersion. It should be considered that the continuous presence of the electrolyte layer facilitates the formation of γ -FeOOH²¹. With the increase in immersion time, the phase composition remained consistent, while the α -FeOOH peak value increased significantly. A semi-quantitative analysis (about 10 relative percent errors) has been performed on the X-ray diffractograms to identify the proportion of different phases among the corrosion products^{22,23}. As shown in Fig. 12, with the immersion, the proportion of α -FeOOH was increased gradually, especially after immersion for 60 days. It indicates that with the increase in immersion time, the protection of the rust layer is gradually enhanced, thus reducing the corrosion of the substrate.

The composition and valence of the main alloy elements (Ni, Cr, and Mo) in the corrosion product formed on the surface of three samples were analyzed by XPS. The fitting results are presented in Fig. 13. The Ni presents in one chemical state, assigned to $\text{Ni}(\text{OH})_2$ or NiFe_2O_4 (855.5 eV)^{24,25}, which is difficult to distinguish from the state of oxide due to their close peak positions. However, $\text{Ni}(\text{OH})_2$

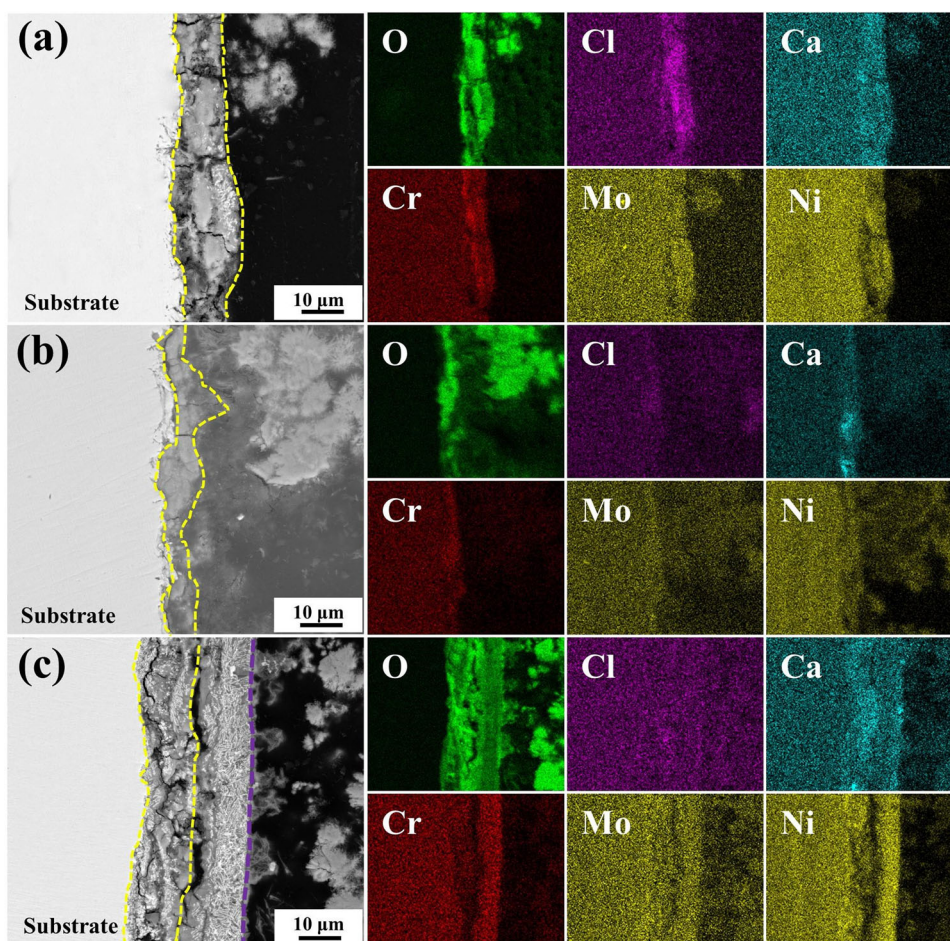


Fig. 7 Cross-sectional morphology and element distribution of corrosion product layers on the (a) Q sample, (b) QT sample, and (c) QLT sample after immersion for 30 days, respectively.

is the main product in the long-term immersion solution, while NiFe_2O_4 is detected in the spectra of Fe 2p_{3/2}, so there are two states for Ni, namely $\text{Ni}(\text{OH})_2/\text{NiFe}_2\text{O}_4$. Similarly, the spectrum peak of Mo is not obvious, which indicates that the content of Mo in corrosion products is relatively low, and the Mo 3d_{5/2} spectrum is mainly divided into FeMoO_4 (231.7 eV)^{26,27}. According to the results, the composition of the corrosion product mainly contained NiFe_2O_4 , FeOOH , $\text{Ni}(\text{OH})_2$, and FeMoO_4 , which means the compounds in the corrosion product layer among the three samples are the same. As for Cr, there is no obvious peak in the spectrum, which indicates that there are few products containing Cr in the corrosion products. In summary, the composition and valence of the main alloy elements (Ni, Cr, and Mo) in the corrosion product show little difference among three samples with various microstructures and retained austenite.

Electrochemical measurements

Figure 14a shows the potentiodynamic polarization measurements of Q, QT, and QLT samples. It can be seen from the results that the three heat-treated steels showed similar electrochemical behavior. The cathodic part of the polarization curves shows no difference in the cathodic process. The change in corrosion potential and current density of three specimens is displayed in Fig. 14b. A comparison of three polarization curves shows that the corrosion potential increased from $-670 \text{ mV}_{\text{vs.SCE}}$ to $-640 \text{ mV}_{\text{vs.SCE}}$, while the current density shows a trend of first decrease and then increase. The corrosion current density of the QT sample is about

$7.26 \mu\text{A}/\text{cm}^2$, which indicates that the QT sample has better corrosion resistance.

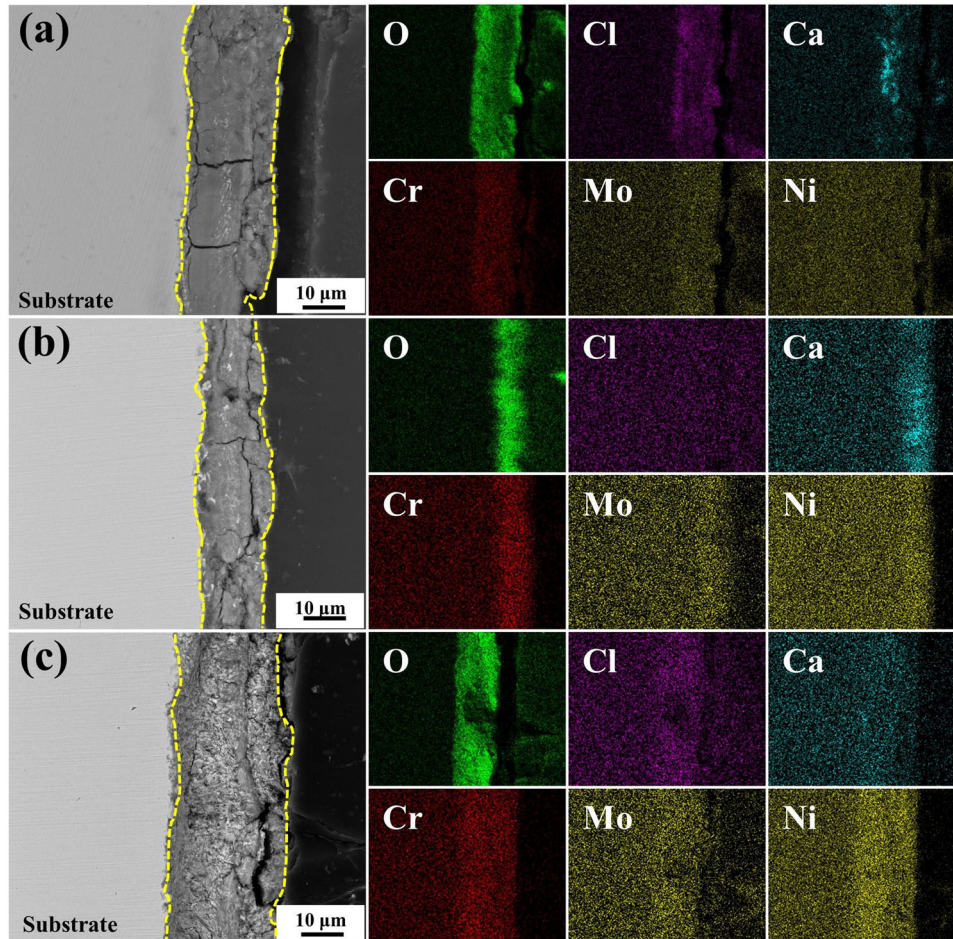
Figure 15 shows the electrochemical impedance results of three samples in artificial seawater at room temperature. The Nyquist plots show similar features, which include only one capacitive arc. Generally, the QT sample has the largest radius of capacitive arc, showing the best corrosion resistance. The EIS data are fitted using the $R(Q(R(QR)))$ equivalent circuit diagram, where R_s is the solution resistance, Q_f is the capacitance of the surface corrosion product film. Q_{dl} and R_{ct} are the double layer and charge transfer resistance, respectively. Table 1 shows the fitting data from the EIS analysis. R_{ct} can be used to evaluate the corrosion resistance of specimens in a corrosion solution. The R_{ct} values of the Q and QLT samples are similar, which are 1641 and 1611 $\Omega\cdot\text{cm}^2$ respectively. As for the QT sample, the R_{ct} is 2109 $\Omega\cdot\text{cm}^2$. There is a very substantial effect on the corrosion resistance after different heat treatments, which is related to the microstructure and retained/reversed austenite.

Atomic force microscopy measurements

The surface morphology and corresponding Volta potential of the three specimens are characterized using SKPFM. In general, the surface potential is regarded as a criterion^{28–30}. With different heat treatment, the Volta potential between the retained/reversed austenite and matrix would change. The surface morphologies for three samples vary greatly, as illustrated in Fig. 16. The Volta potential of grain boundaries, lath borders, and pocket borders is higher than that of the matrix. Blocky and film retained austenite

Table 1. Electrochemical impedance spectrum fitting results for the Q, QT, and QLT specimens.

| Steel | $R_s/\Omega\cdot\text{cm}^2$ | $Q_f \times 10^{-4}/\Omega^{-1} \text{cm}^{-2} \text{s}^n$ | n_f | $R_p/\Omega\cdot\text{cm}^2$ | $Q_{dl} \times 10^{-4}/\Omega^{-1} \text{cm}^{-2} \text{s}^n$ | n_1 | $R_{ct}/\Omega\cdot\text{cm}^2$ |
|-------|------------------------------|--|--------|------------------------------|---|--------|---------------------------------|
| Q | 7.82 | 3.49 | 0.8127 | 71.65 | 1.72 | 0.8501 | 1641 |
| QT | 7.24 | 7.65 | 0.7738 | 12.17 | 3.04 | 0.9626 | 2109 |
| QLT | 7.71 | 2.07 | 0.8607 | 39.39 | 1.39 | 0.8743 | 1611 |

**Fig. 8** Cross-sectional morphology and element distribution of corrosion product layers on the (a) Q sample, (b) QT sample, and (c) QLT sample after immersion for 60 days, respectively.

is also observed both at the lath boundary and pocket borders, which have a noble Volta potential than the matrix, just as shown in Fig. 16b₂. For the QLT sample, Fig. 16c₂ obviously shows that the reversed austenite is uniformly distributed and has a higher Volta potential.

Figure 17 shows the morphology and Volta potential profile of lines. For the Q sample, the Volta potential of the lath boundary and the PAGB is approximately 29 mV higher than that of the matrix. According to the analysis of both lines A and B of QT sample, the potential distribution of blocky retained austenite is uneven, and the local zone has a higher Volta potential. The measured potential is 36 mV compared to the reversed austenite. For the QLT sample, the RA has a higher Volta potential than the matrix, while at the RA/matrix interface, there existed a low potential area (as shown by the arrow in Fig. 17d). Detailed analysis of the local potential difference reveals a value of 56 mV. Experimental observations and theoretical studies indicated that the Volta potential had a linear relationship with the corrosion potential in solution. The lower potential areas

would be more prior to corrode³¹. This result indicated that the interface between the RA and matrix may be a position of priority corrosion nucleation²⁸. Similarly, the interface between the lath boundary or PAGB and matrix may be susceptible to corrode. To sum up, heat treatment significantly changes the potential distribution of tissues.

DISCUSSION

It is extremely complex and diverse to explain the influence of microstructure on corrosion origin. Many studies have shown that the initiation of local corrosion in low alloy steel is closely related to the micro-nano scale texture in the steel, such as inclusions, microstructure, precipitates, and defects^{4,8,10,12,20,32,33}. The microstructure and phase structure are considered to have an important effect on the corrosion behavior of steel after different heat treatment conditions^{34–38}. The microstructure of the NiCrMoV/Nb steel obtained by heat treatment mainly contained martensite and

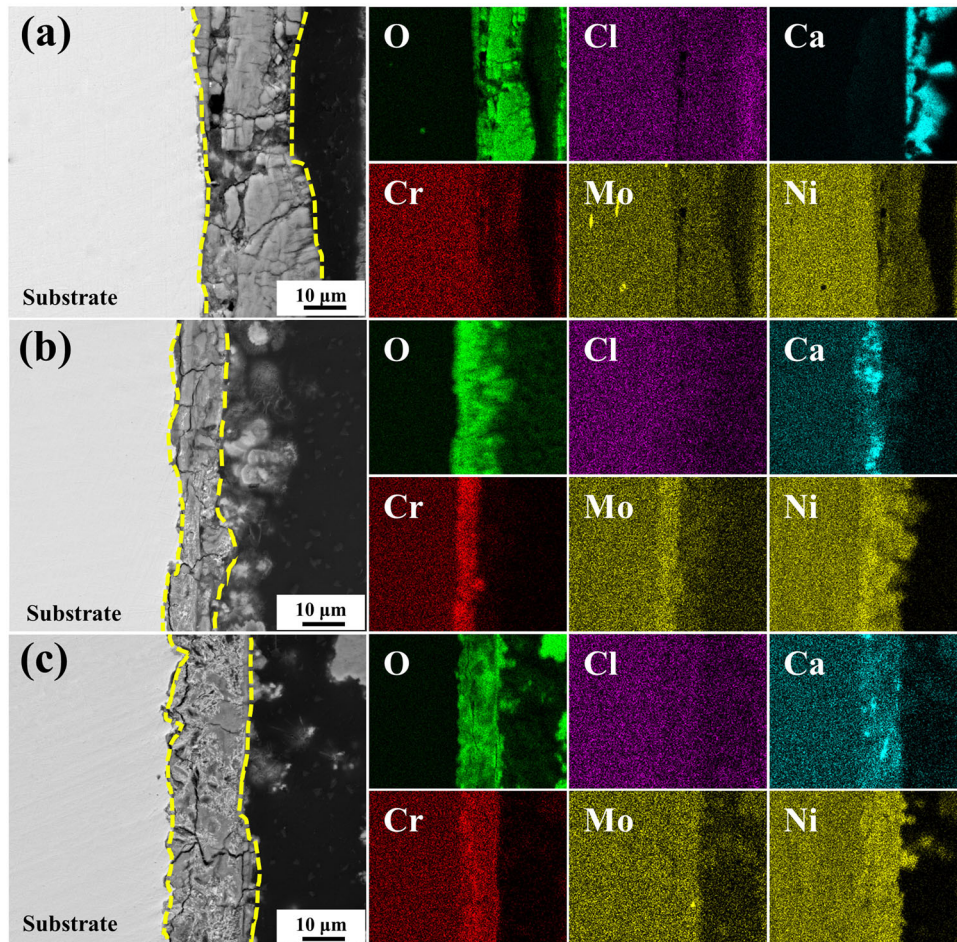


Fig. 9 Cross-sectional morphology and element distribution of corrosion product layers on the (a) Q sample, (b) QT sample, and (c) QLT sample after immersion for 90 days, respectively.

a certain amount of reverse austenite. Therefore, the relationship among microstructure, reverse austenite, and corrosion behavior is discussed in detail.

Effect of the microstructure and reverse austenite on corrosion resistance of steel matrix

Generally speaking, the quenched steel contained a single martensite structure, which demonstrates better corrosion resistance than a complex phase^{39–42}. The potential of the grain boundary, lath borders, and pocket borders is 29 mV higher than that of the matrix. When the steel is tempered, the retained austenite is generated at the grain boundaries and lath borders and has a 36 mV higher potential than that of the matrix. The size of the retained austenite is refined, and its distribution is more uniform after double tempering heat treatment. The difference in Volta potential between the retained austenite and the matrix gradually increases to 56 mV. The change in heat treatment increases the potential difference between the retained austenite and the matrix, which intensifies the corrosion tendency of the area with a lower potential (Fig. 5)⁸. Based on the test results and SKPFM test results (Figs. 16 and 17), we summarize several important reasons for the influence of RA on corrosion behavior.

On the one hand, the nickel, and carbon enrichment in retained austenite increase the Volta potential, mainly due to the noble electrode potential^{13,22,25,39,43,44}. The retained austenite as cathode phase will form a large anode and a small cathode under this condition, which will reduce corrosion. When double tempering

heat treatment is adopted, the content of reverse austenite increases to 13.8%. With the increase of the content of reverse austenite, the area of the cathode phase increases, reducing the area ratio of the cathode to the anode, which could promote the corrosion tendency of the matrix.

On the other hand, the enrichment degree of the Ni element in the reverse austenite increases due to the longer tempering time and the more sufficient diffusion of elements. The chemical heterogeneities promoted an approximately 56 mV potential difference, which has a stronger microgalvanic effect and could accelerate the corrosion. Experimental observations and theoretical studies indicated that, according to the previous paper^{31,45}, the Volta potential had a linear relationship with the corrosion potential in solution. The lower potential areas would be more susceptible to corrosion. Therefore, the interface between the retained austenite and the matrix is the low potential area, where pits are easy to nucleate (as shown in Fig. 5). Considering the decrease in residual stress and the relatively small amount of retained austenite in tempered steel, the QT sample shows good corrosion resistance. Furthermore, based on the immersion results (Figs. 5 and 6), we also conclude that the pits mainly nucleated at the reverse austenite/matrix interface.

In summary, the quenched specimen is a single martensite structure with a high density of dislocations and residual stresses in the tissue. The higher electrochemical activity results in a higher corrosion rate. As for the QLT specimen, the chemical heterogeneities promoted a higher potential difference, which has a stronger microgalvanic effect and could accelerate the corrosion. Thus, it exhibits the worst corrosion resistance (Figs. 6 and 14).

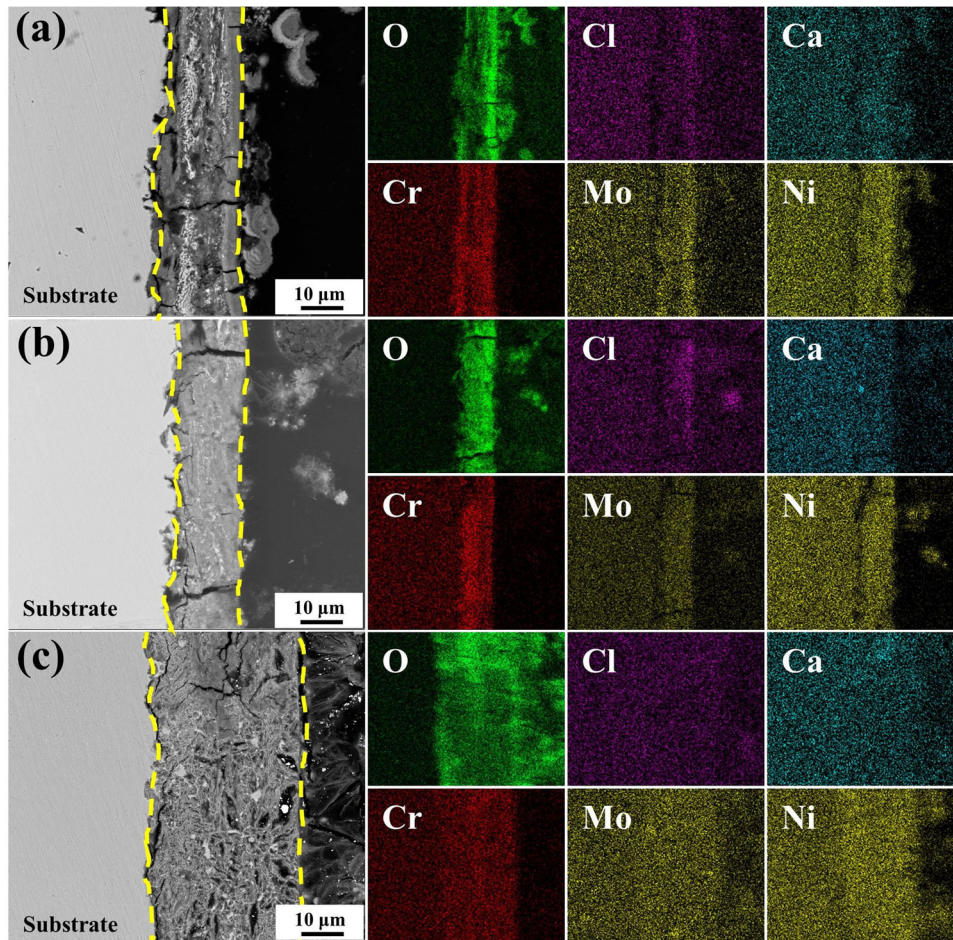
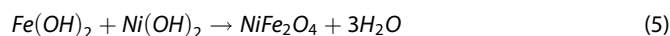
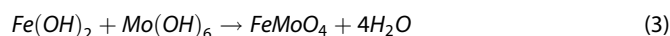
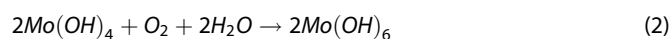


Fig. 10 Cross-sectional morphology and element distribution of corrosion product layers on the (a) Q sample, (b) QT sample, and (c) QLT sample after immersion for 180 days, respectively.

In consideration of the low carbon content in steel and the formation of the retained austenite, the precipitation of the carbide is inhibited, which may have a relatively small impact on the resistance compared to the retained austenite. Thus, the effect of precipitation on corrosion resistance could be ignored in this paper.

Effect of the microstructure and retained austenite on evolution of corrosion product layer

Generally, the formation of corrosion products may affect the corrosion behavior of steel substrates. Figure 18 illustrates the corrosion mechanism of NiCrMoV/Nb steel in the artificial seawater. The metal atoms are gradually dissolved and from various metallic ions in the initial stage of corrosion, as shown in Fig. 18a. These cations may hydrolyze to form some hydroxides as well as complex oxides. These reactions, which are illustrated below, have been discussed in some publications.



During the rust formation, the inhomogeneity and the microstructure and elements may affect the corrosion process. On the one hand, as has been discussed above, the nickel and carbon enrichment in retained austenite increase the volta potential mainly due to the noble electrode potential. The microgalvanic effect between the reversed austenite and matrix accelerates the corrosion of the matrix around RA, as shown in Fig. 18b. On the other hand, since all samples have the same composition and contain alloying elements such as Ni, Cr, Mo, etc., the different contents of the Ni element in the retained austenite and matrix may also cause differences in the corrosion product⁴⁶ (Figs. 11 and 12).

After the steel surface has been fully covered by corrosion product, it prevents the majority of the corrosive medium from contacting the substrate. The corrosion product layer (CPL), which forms in seawater as opposed to the marine environment, is loose and delivers less protection^{14,22,27,47,48}. (Figs. 7–9) A sufficient amount of solution can still transform the corrosion product layer through structural defects, such as cracks and pores. This process is briefly displayed in Fig. 18c. Thus, the protection of CPL is an important effect factor in the late stage of corrosion. XRD and XPS results confirm the existence of $\text{Ni}(\text{OH})_2/\text{NiFe}_2\text{O}_4$, FeMoO_4 and FeOOH . Previous studies reported^{22,49} that the addition of Ni to steel is conducive to the formation of nanostructure NiFe_2O_4 , which can promote the nucleation and growth of Fe (O, OH)₆ nano-network structure. It is conducive to the formation of a protective rust layer. Similarly^{50–52}, addition of Mo can form

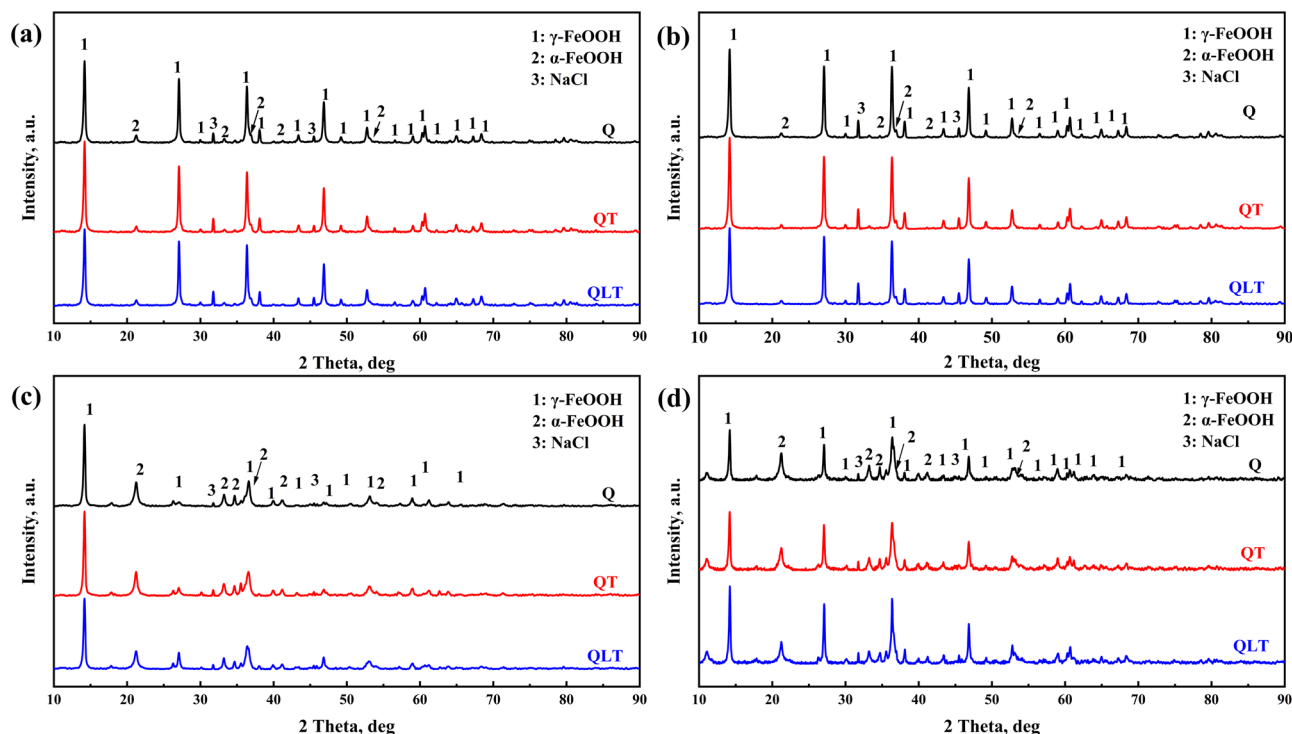


Fig. 11 The phase composition of corrosion product layers on the Q, QT and QLT samples after immersion for (a) 30 days, (b) 60 days, (c) 90 days, and (d) 180 days, respectively.

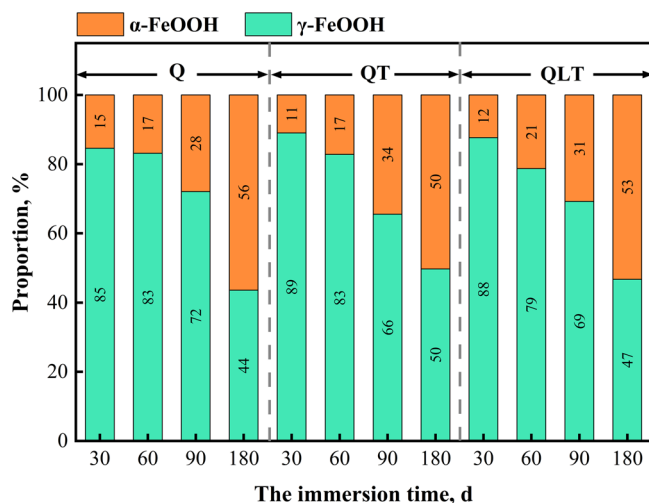


Fig. 12 The proportion of each phase of the Q, QT, and QLT samples after immersion for different time.

MoO_4^{2-} in solution. As a typical anodic corrosion inhibitor, MoO_4^{2-} preferentially adsorb on the steel surface, which can isolate the adsorption position of Cl^- in order to inhibit the active dissolution of steel. Thus, the nickel enrichment in rust layer promoted the formation of $\alpha\text{-FeOOH}$, it gradually accumulates in the interface of the steel with the increase of immersion. This process is described in Fig. 18d. The proportion of $\alpha\text{-FeOOH}$ is lower due to local Ni enrichment, which leads to the reduction of Ni content in the matrix. Thus, lower contain of nickel in the rust layer is alleviated to the formation and conversion of $\alpha\text{-FeOOH}$ (Fig. 12). The rust layer with dense and higher protective components has the best protection performance.

Table 2. Chemical composition of NiCrMoV steel (wt. %).

| C | Si | Mn | P | S | Ni | Cr | Mo | V | Nb | Fe |
|-------|------|------|-------|--------|------|------|------|-------|-------|------|
| 0.043 | 0.30 | 0.81 | 0.004 | 0.0039 | 7.97 | 0.60 | 0.59 | 0.080 | 0.032 | Bal. |

METHODS

Materials and sample preparation

The test materials what used in this work were provided by Angang Steel Company. The chemical compositions of steel are listed in Table 2. The steel was smelted in a 50 kg vacuum smelting furnace under the protection of argon gas. The steel ingots were homogenized at 1200 °C for 2 hours and then rolled at a temperature of 1050 °C. A thickness of 12 mm plate was obtained after 12 times of rolling, and then cooled to room temperature using the automatic water-cooling system. All the specimens were sub-heated at 840 °C for 1 hour and then water cooled. Critical temperatures Ac1 and Ac3 were measured to be 658 and 748 °C by the standard. Three heat treatments (as shown in Table 3) were performed to obtain various retained/reversed morphologies. The intercritical temperature was selected at 660 °C according to previous research findings. The samples were hereafter marked as Q, QT, and QLT, respectively.

Microstructural characterization

Sample microstructures were characterized using a SEM (FEI Quant 250) after etching with a 4% nital solution. Transmission electron microscopy (TEM, JEOL-2100F) was applied to determine the fine structure of the matrix. A 0.5-mm-thick sample, mechanically ground to about 50 μm, was prepared for TEM observation. The sample was twin-jet polished with 5 vol% perchloric acid and 95 vol% alcohol at 25 V. Additionally, volume fractions of the retained austenite were measured by X-ray

diffraction (Rigaku, Smartlab9kw) from a Rietveld analysis, where the scan range was 30–90° and the scanning rate was selected at 1°/min. The volume fraction of retained/reversed austenite was

evaluated using the following equation⁵³.

$$V_{\alpha'} + V_{\gamma} = 1 \quad (6)$$

$$V_{\gamma} = \frac{1.4I_{\gamma}}{I_{\alpha'} + 1.4I_{\gamma}} \quad (7)$$

where $V_{\alpha'}$ and V_{γ} are the volume fraction of martensite and retained/reversed austenite, respectively. $I_{\alpha'}$ and I_{γ} are the integrated intensities of $(1\ 1\ 0)_{\alpha'}$ and $(1\ 1\ 1)_{\gamma}$ peak, respectively.

Electrochemical measurements

The electrochemical measurements were taken by a 3F electrochemical workstation in an artificial seawater solution using a traditional three-electrode cell system. A Pt plate was applied as the counter electrode, a saturated calomel electrode (SCE) was used as the reference electrode, and the three specimens were the working electrode. The scan rate of the polarization curve was

| Condition | Heat treatment | Temperature (°C) | Time (h) |
|-----------|---|---------------------|-------------|
| Q | Solution quenching | 840 | 1 |
| QT | Solution quenching +tempering | 840 +600 | 1 2 |
| QLT | Solution quenching +double tempering | 840+ 660+ 600 | 1 1 2 |

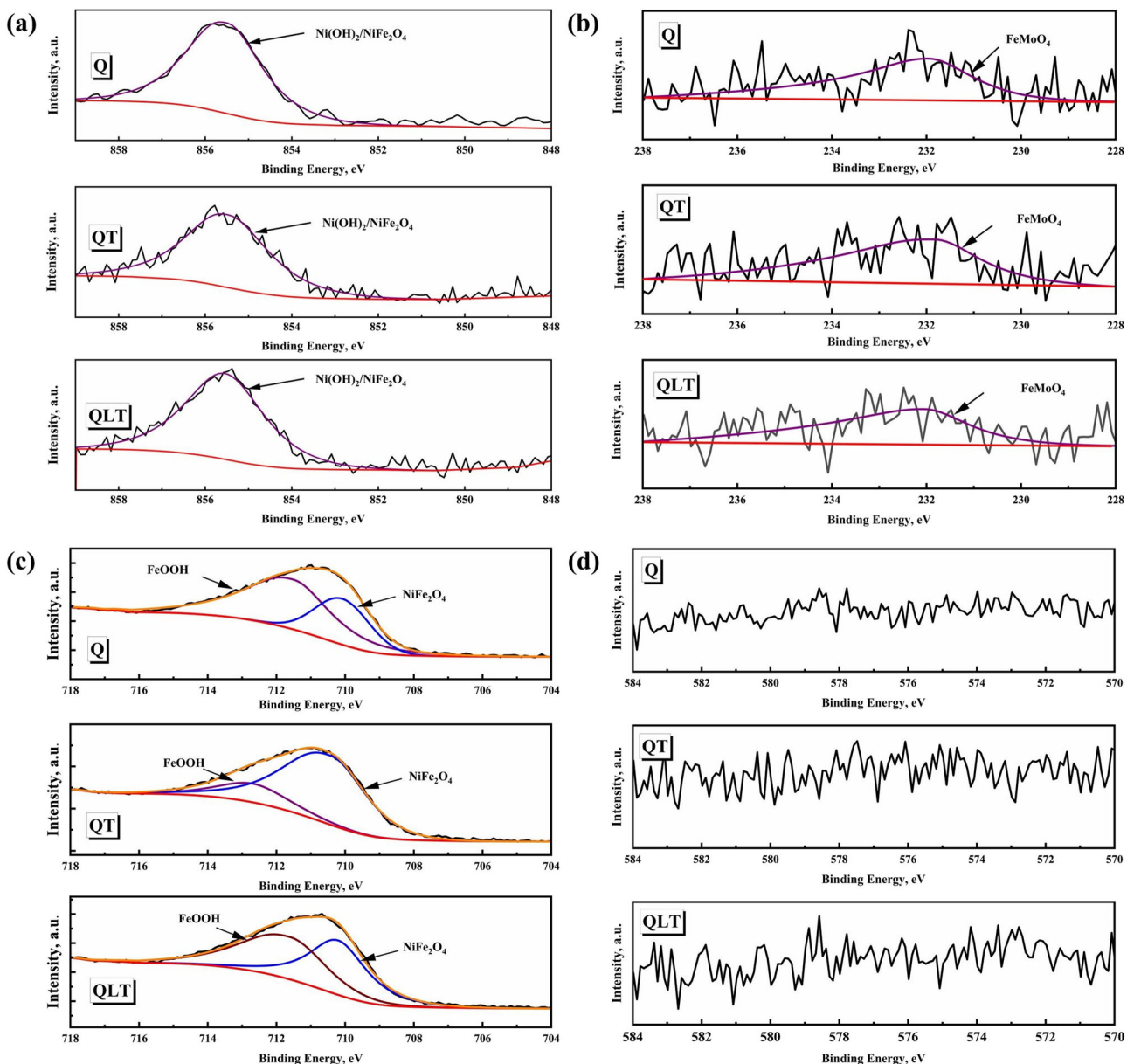


Fig. 13 XPS spectra of the corrosion products layer on the steels after immersion for 90 days. **a** Ni $2p_{3/2}$, **b** Mo $3d_{5/2}$, **c** Fe $2p_{3/2}$, and **d** Cr $2p_{3/2}$.

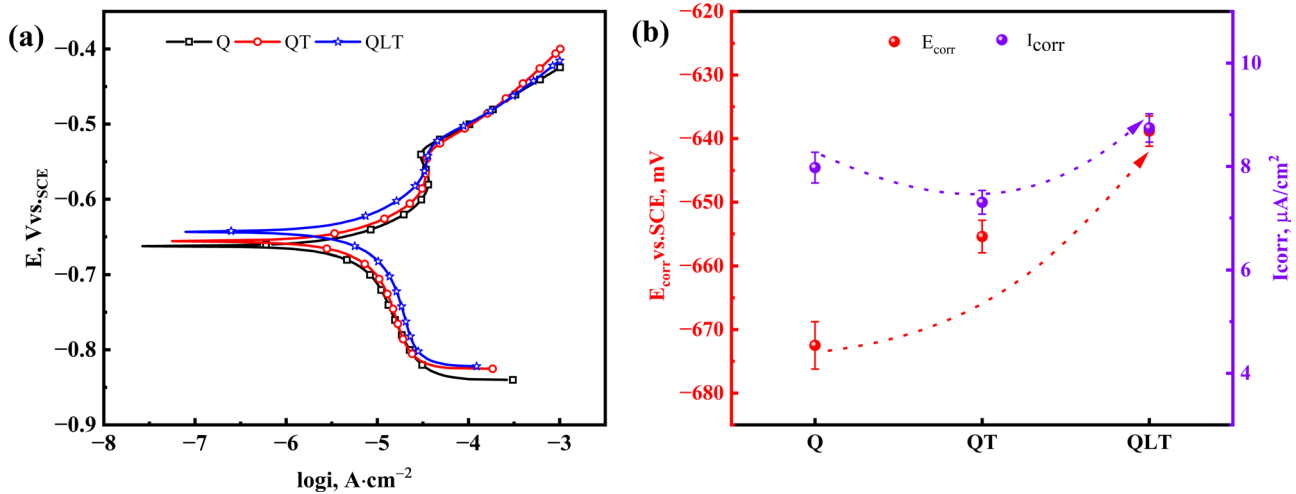


Fig. 14 Potentiodynamic polarization curves (a) and (b) the corresponding electrochemical parameters of Q, QT and QLT specimens.

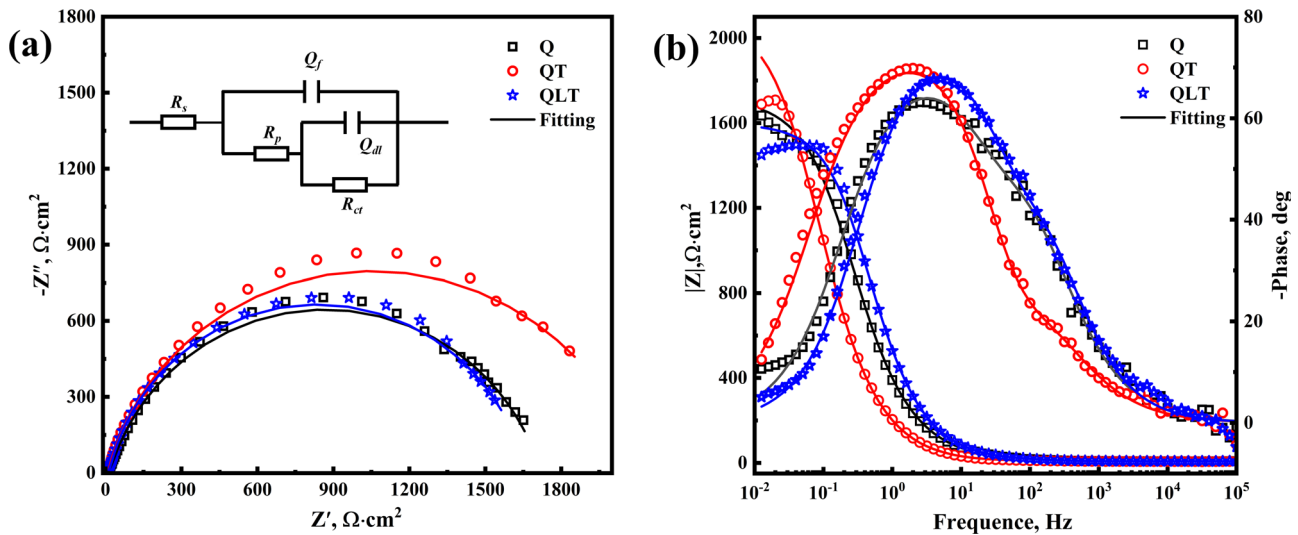


Fig. 15 EIS curves of Q, QT, and QLT specimens. a Nyquist, b Bode plots.

0.5 mV/s. The frequency of electrochemical impedance spectroscopy (EIS) measurements was 10 mHz–100 kHz and the amplitude were 10 mV. Before conducting the electrochemical test, the system was allowed to stabilize for 60 min at a solution temperature of 25 °C.

Immersion test

Immersion test is a reliable and simple method for analyzing the localized corrosion mechanism in the early stage of the corrosion process. For the immersion tests, an aqueous solution (pH = 8.2) contained 24.53 g/L NaCl, 5.20 g/L $MgCl_2$, 4.09 g/L Mg_2SO_4 , 1.16 g/L $CaCl_2$, 0.695 g/L KCl, 0.201 g/L $NaHCO_3$, 0.101 g/L KBr, 0.027 g/L H_3BO_3 , 0.025 g/L $SrCl_2$, and 0.003 g/L NaF. Prior to examination of the corrosion morphology, a solution containing HCl and hexamethylenetetramine was used to remove the rust, and then the specimens were washed with alcohol and dried with pressurized air. Besides, the corrosion morphology of the samples after removing the rust was observed by the FE-SEM (GeminiSEM500).

The original weight and surface area were recorded for all the samples prior to long immersion, and then the samples were immersed in the test solution for 30, 60, 90 and 180 days. After immersion finished, the samples were taken out and weighed

after removing the surface corrosion products. The corrosion rates (R) of three samples were calculated as the following:

$$R = \frac{(W_0 - W_t) \times 10^4}{Spt} \quad (8)$$

Where W_0 and W_t are the original weight of samples before immersion and in different immersing period, respectively, g; S represents the exposed area of each sample, cm^2 . ρ is the density of the steels, $7.8 g/cm^3$. t is the immersion time, y.

Analysis of composition of corrosion product layer

The cross-sectional morphologies of the corrosion product layer were observed in detail by SEM. XRD analysis was applied to identify the crystalline phase in corrosion products with a 10–90° scan range and a 5°/min scanning rate. Additionally, the presence states of main alloying elements (Ni, Cr, and Mo) in corrosion products were investigated by the XPS (Thermo ESCALAB 250XI) technique with an Al K α X-ray radiation source. All the binding energy was calibrated with the peak of C1s (284.6 eV).

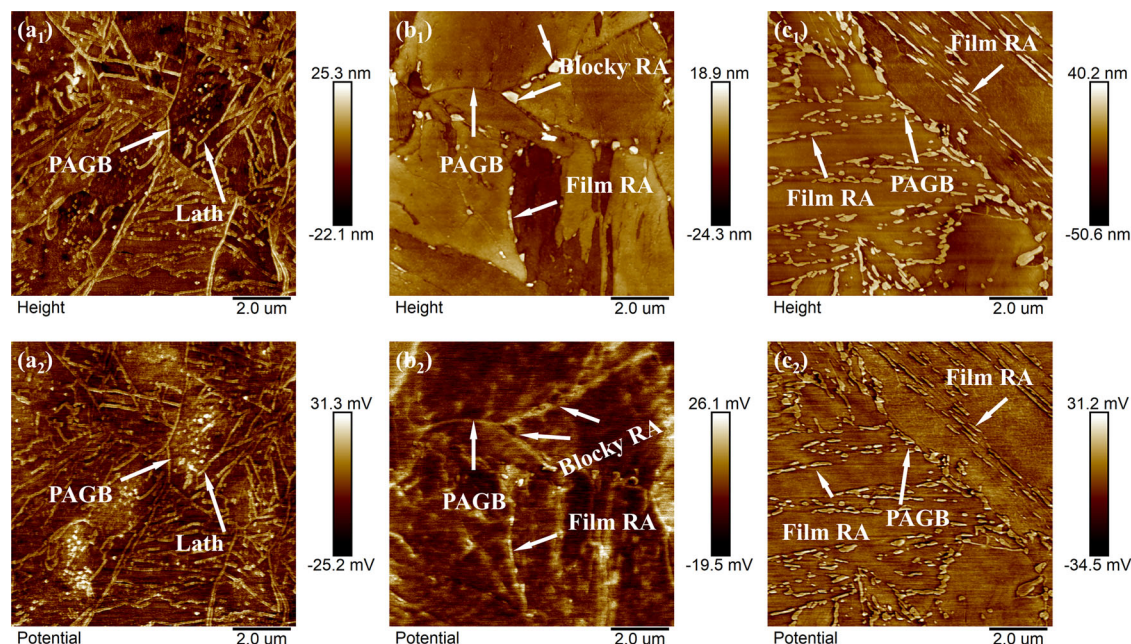


Fig. 16 SKPFM analysis of three specimens. a Q, b QT, c QLT. a₁, b₁, c₁ Surface topography, a₂, b₂, c₂ Surface Volta potential.

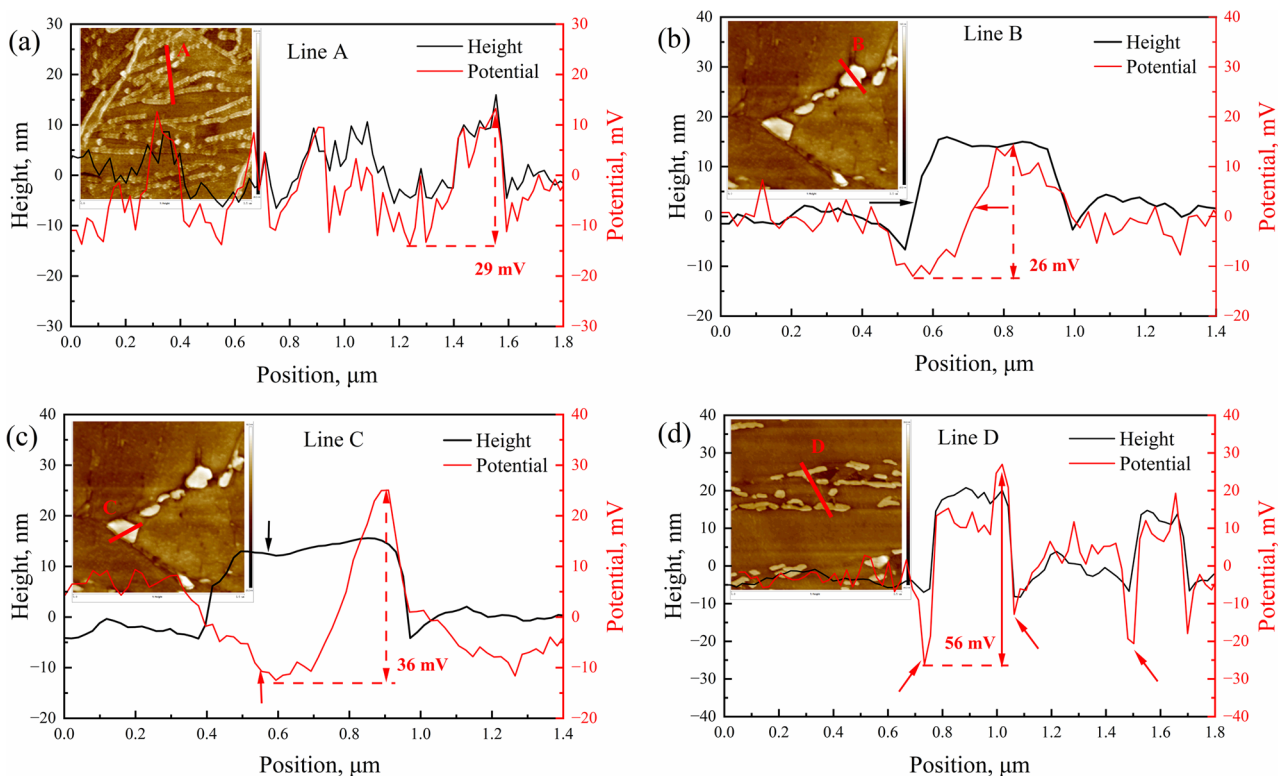


Fig. 17 SKPFM topography and line profile analyses for selected areas. a Q sample, b, c QT sample, d QLT sample.

Atomic force microscopy measurements

The Volta potential and morphology of the microstructures were measured by a commercial AFM (Bruker MultiMode 8, Germany). Volta potential images of 10 μm by 10 μm were successively obtained with a scan rate of 0.498 Hz. All SKPFM measurements were taken in the tapping mode in air at 25 $^{\circ}\text{C}$ room temperature. After scanning, the Volta potential images were mathematically

inverted by the software NanoScope Analysis 2.0 in order to conform to the electrochemical convention. Therefore, the relationship between the contact potential difference (i.e., the Volta potential) measured in this study and the work function difference was defined as⁵⁴:

$$\Delta V_{\text{CPD}} = V_{\text{tip}} - V_{\text{sample}} = (\varphi_{\text{sample}} - \varphi_{\text{tip}})/e. \quad (9)$$

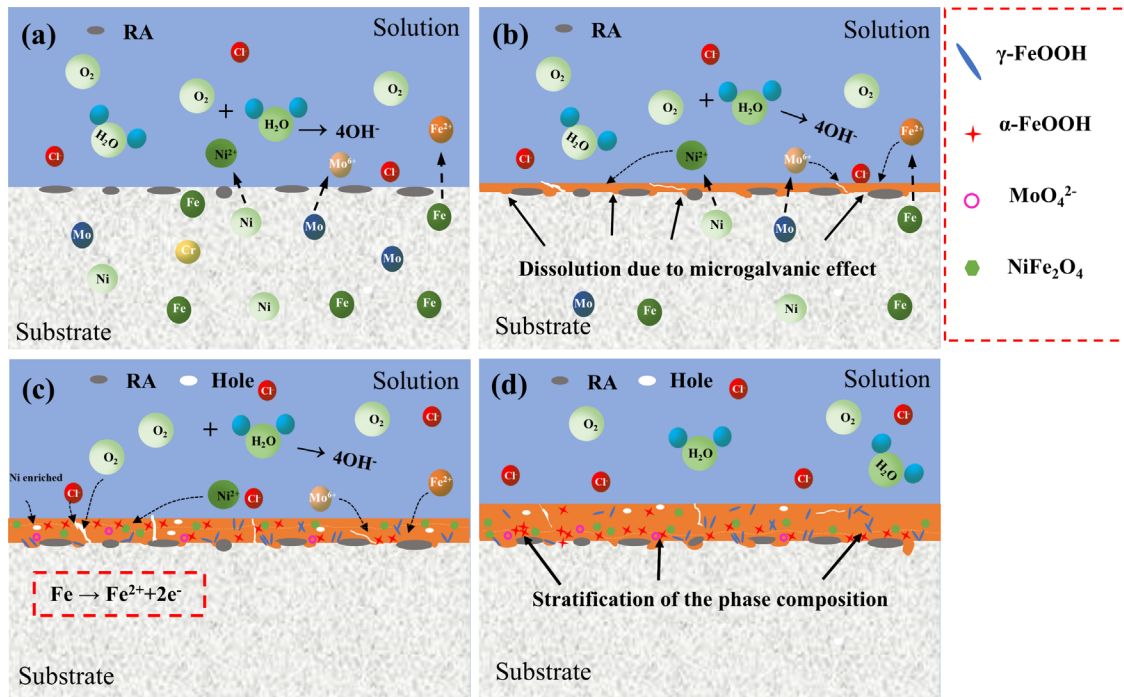


Fig. 18 The corrosion mechanism of NiCrMoV/Nb steel in the artificial seawater.

where ϕ_{sample} and ϕ_{tip} are the work functions of tip and sample, respectively, ΔV_{CPD} is the contact potential difference between the tip and sample, and e is the elementary charge⁴².

DATA AVAILABILITY

The data that support the findings of this study are available from the corresponding authors upon reasonable request.

Received: 21 February 2023; Accepted: 3 May 2023;
Published online: 23 May 2023

REFERENCES

- Robert, C. & Voigt Analysis of intercritical heat treatment of cast steels. *J. Iron Steel Res. Int.* **17**, 44–50 (2010).
- Yang, Y., Cai, Q., Wu, H. & Wang, H. Formation of reversed austenite and its effect on cryogenic toughness of 9Ni steel during two-phase region heat treatment. *Acta Metall. Sin.* **45**, 270–274 (2009).
- Zhu, X., Li, W., Zhao, H. G., Wang, L. & Jin, X. Hydrogen trapping sites and hydrogen-induced cracking in high strength quenching & partitioning (Q&P) treated steel. *J. Hydrog. Energy* **39**, 13031–13040 (2014).
- Vignal, V., Krawiec, H., Heintz, O. & Oltra, R. The use of local electrochemical probes and surface analysis methods to study the electrochemical behaviour and pitting corrosion of stainless steels. *Electrochim. Acta* **52**, 4994–5001 (2007).
- Song, Y., Cui, J. & Rong, L. Microstructure and mechanical properties of 06Cr13Ni4Mo steel treated by quenching-tempering-partitioning process. *J. Mater. Sci. Technol.* **32**, 189–193 (2016).
- Song, Y., Li, X., Rong, L. & Li, Y. The influence of tempering temperature on the reversed austenite formation and tensile properties in Fe-13%Cr-4%Ni-Mo low carbon martensitic stainless steels. *Eng. A.* **528**, 4075–4079 (2011).
- Man, C., Dong, C., Xiao, K., Yu, Q. & Li, X. The combined effect of chemical and structural factors on pitting corrosion induced by MnS-(Cr, Mn, Al)O duplex inclusions. *Corrosion* **74**, 312–325 (2018).
- Liu, C. et al. Effect of inclusions modified by rare earth elements (Ce, La) on localized marine corrosion in Q460NH weathering steel. *Corros. Sci.* **129**, 82–90 (2017).
- Tewary, N. K., Kundu, A., Nandi, R., Saha, J. K. & Ghosh, S. K. Microstructural characterisation and corrosion performance of old railway girder bridge steel and modern weathering structural steel. *Corros. Sci.* **113**, 57–63 (2016).
- Torkkeli, J., Saukkonen, T. & Hanninen, H. Effect of MnS inclusion dissolution on carbon steel stress corrosion cracking in fuel-grade ethanol. *Corros. Sci.* **96**, 14–22 (2015).
- Shibaeva, T. V., Laurinavichyute, V. K., Tsirlina, G. A., Arsenkin, A. M. & Grigorovich, K. V. The effect of microstructure and non-metallic inclusions on corrosion behavior of low carbon steel in chloride containing solutions. *Corros. Sci.* **80**, 299–308 (2014).
- Krawiec, H., Vignal, V. & Oltra, R. Use of the electrochemical microcell technique and the SVET for monitoring pitting corrosion at MnS inclusions. *Electrochem. Commun.* **6**, 655–660 (2004).
- Wu, W., Qin, L., Cheng, X., Xu, F. & Li, X. Microstructural evolution and its effect on corrosion behavior and mechanism of an austenite-based low-density steel during aging. *Corros. Sci.* **212**, 110936 (2023).
- Ma, H. et al. Stress corrosion cracking of E690 steel as a welded joint in a simulated marine atmosphere containing sulphur dioxide. *Corros. Sci.* **100**, 627–641 (2015).
- Franceschi, M. et al. Effect of different austempering heat treatments on corrosion properties of high silicon steel. *Mater.* **14**, 2 (2021).
- Hsu, C. & Chen, M. Corrosion behavior of nickel alloyed and austempered ductile irons in 3.5% sodium chloride. *Corros. Sci.* **52**, 2945–2949 (2010).
- Vignal, V. et al. Influence of the microstructure on the corrosion behaviour of low-carbon martensitic stainless steel after tempering treatment. *Corros. Sci.* **85**, 42–51 (2014).
- Bilmes, P. D., Llorente, C. L., Mendez, C. M. & Gervasi, C. A. Microstructure, heat treatment and pitting corrosion of 13CrNiMo plate and weld metals. *Corros. Sci.* **51**, 876–881 (2009).
- Bilmes, P. D., Llorente, C. L., Huaman, L. S., Gassa, L. M. & Gervasi, C. A. Microstructure and pitting corrosion of 13CrNiMo weld metals. *Corros. Sci.* **48**, 3261–3270 (2006).
- Liu, C. et al. Influence of rare earth metals on mechanisms of localised corrosion induced by inclusions in Zr-Ti deoxidised low alloy steel. *Corros. Sci.* **166**, 108463 (2020).
- Tian, H. et al. Corrosion evolution and stress corrosion cracking behavior of a low carbon bainite steel in the marine environments: Effect of the marine zones. *Corros. Sci.* **206**, 110490 (2022).
- Cheng, X., Jin, Z., Liu, M. & Li, X. Optimizing the nickel content in weathering steels to enhance their corrosion resistance in acidic atmospheres. *Corros. Sci.* **115**, 135–142 (2017).
- Hubbard, C. R. & Snyder, R. L. RIR - measurement and use in quantitative XRD. *Powder Diff.* **3**, 74–77 (1988).
- Jia, J., Wu, W., Cheng, X. & Zhao, J. Ni-advanced weathering steels in Maldives for two years: corrosion results of tropical marine field test. *Constr. Build. Mater.* **245**, 118463 (2020).

25. Wang, L. et al. The effect of η -Ni₃Ti precipitates and reversed austenite on the passive film stability of nickel-rich Custom 465 steel. *Corros. Sci.* **154**, 178–190 (2019).
26. Zhang, Z. et al. Synthesis and magnetic property of FeMoO₄ nanorods. *Mat. Sci. Eng. B.* **176**, 756–761 (2011).
27. Sun, M. et al. Distinct beneficial effect of Sn on the corrosion resistance of Cr-Mo low alloy steel. *J. Mater. Sci. Technol.* **81**, 175–189 (2021).
28. Davoodi, A., Pan, J., Leygraf, C. & Norgren, S. In situ investigation of localized corrosion of aluminum alloys in chloride solution using integrated EC-AFM/SECM techniques. *Electrochem. Solid State Lett.* **8**, 21–24 (2005).
29. Stratmann, M. & Streckel, H. On the atmospheric corrosion of metals which are covered with thin electrolyte layers—II. Experimental results. *Corros. Sci.* **30**, 697–714 (1990).
30. Yee & Shelton Application of a Kelvin microprobe to the corrosion of metals in humid atmospheres. *J. Electrochem. Soc.* **138**, 55–61 (1991).
31. Davoodi, A., Pan, J., Leygraf, C. & Norgren, S. Integrated AFM and SECM for in situ studies of localized corrosion of Al alloys. *Electrochim. Acta* **52**, 7697–7705 (2007).
32. Li, G. et al. Dissolution kinetics of the sulfide-oxide complex inclusion and resulting localized corrosion mechanism of X70 steel in deaerated acidic environment. *Corros. Sci.* **174**, 108815 (2020).
33. Lu, Q. et al. Corrosion evolution and stress corrosion cracking of E690 steel for marine construction in artificial seawater under potentiostatic anodic polarization. *Constr. Build. Mater.* **238**, 117763 (2020).
34. Wang, L. et al. In situ corrosion characterization of simulated weld heat affected zone on API X80 pipeline steel. *Corros. Sci.* **85**, 401–410 (2014).
35. Guo, Y. et al. Effect of microstructure variation on the corrosion behavior of high-strength low-alloy steel in 3.5wt% NaCl solution. *Int. J. Miner., Metall. Mater.* **22**, 604–612 (2015).
36. Shaopo, L. I., Jia, G. U. O., Shanwu, Y. & Xinlai, H. E. Effect of carbon content and microstructure on the corrosion resistance of low alloy steels. *J. Univ. Sci. Technol. Beijing* **30**, 16–20 (2008).
37. Clover, D., Kinsella, B., Pejčić, B. & De Marco, R. The influence of microstructure on the corrosion rate of various carbon steels. *J. Appl. Electrochem* **35**, 139–149 (2005).
38. Hao, X. et al. Effect of tempering temperature on the microstructure, corrosion resistance, and antibacterial properties of Cu-bearing martensitic stainless steel. *Mater. Corros.* **72**, 1668–1676 (2021).
39. Hai, C., Cheng, X., Du, C. & Li, X. Role of martensite structural characteristics on corrosion features in Ni-advanced dual-phase low-alloy steels. *Acta Metall. Sin.* **34**, 802–812 (2021).
40. Ma, C., Peng, Q., Mei, J., Han, E.-H. & Ke, W. Microstructure and corrosion behavior of the heat affected zone of a stainless steel 308L-316L weld joint. *J. Mater. Sci. Technol.* **34**, 1823–1834 (2018).
41. Geng, Y. et al. Effect of laser shock peening on residual stress, microstructure and hot corrosion behavior of damage-tolerant TC2. *1 Titan. alloy. J. Mater. Eng. Perform.* **27**, 4703–4713 (2018).
42. Zhang, C., Cai, D., Liao, B., Zhao, T. & Fan, Y. A study on the dual-phase treatment of weathering steel 09CuPcNi. *Mater. Lett.* **58**, 1524–1529 (2004).
43. Wu, W., Cheng, X., Zhao, J. & Li, X. Benefit of the corrosion product film formed on a new weathering steel containing 3% nickel under marine atmosphere in Maldives. *Corros. Sci.* **165**, 108416 (2020).
44. Milazzo, G., Caroli, S. & Sharma, V. K. *Tables of standard electrode potentials* (Wiley, 1978).
45. Li, M., Guo, L., Qiao, L. & Bai, Y. The mechanism of hydrogen-induced pitting corrosion in duplex stainless steel studied by SKPFM. *Corros. Sci.* **60**, 76–81 (2012).
46. Fratila-Apachitei, L. E., Apachitei, I. & Duszczyk, J. Characterization of cast AlSi(Cu) alloys by scanning Kelvin probe force microscopy. *Electrochim. Acta* **51**, 5892–5896 (2006).
47. Hai, C. et al. Analysis of corrosion evolution in carbon steel in the subtropical atmospheric environment of Sichuan. *J. Mater. Eng. Perform.* **30**, 8014–8022 (2021).
48. Sun, M. et al. Fundamental understanding on the effect of Cr on corrosion resistance of weathering steel in simulated tropical marine atmosphere. *Corros. Sci.* **186**, 109427 (2021).
49. Kimura, M., Kihira, H., Ohta, N., Hashimoto, M. & Senuma, T. Control of Fe(O,OH)(6) nano-network structures of rust for high atmospheric-corrosion resistance. *Corros. Sci.* **47**, 2499–2509 (2005).
50. Mesquita, T. J., Chauveau, E., Mantel, M., Kinsman, N. & Nogueira, R. P. Anomalous corrosion resistance behavior of Mo-containing SS in alkaline media: the role of microstructure. *Mater. Chem. Phys.* **126**, 602–606 (2011).
51. Pardo, A. et al. Effect of Mo and Mn additions on the corrosion behaviour of AISI 304 and 316 stainless steels in H₂SO₄. *Corros. Sci.* **50**, 780–794 (2008).
52. Ilievare, G. O. & Burstein, G. T. The role of alloyed molybdenum in the inhibition of pitting corrosion in stainless steels. *Corros. Sci.* **43**, 485–513 (2001).
53. Morito, S., Tanaka, H., Konishi, R., Furuhashi, T. & Maki, T. The morphology and crystallography of lath martensite in Fe-C alloys. *Acta Mater.* **51**, 1789–1799 (2003).
54. Lacroix, L., Ressler, L., Blanc, C. & Mankowski, G. Statistical study of the corrosion behavior of Al₂CuMg intermetallics in AA2024-T351 by SKPFM. *J. Electrochem. Soc.* **155**, 8–15 (2008).

ACKNOWLEDGEMENTS

This work was supported by the National Materials Corrosion and Protection Data Center and Beijing Advanced Innovation Center for Materials Genome Engineering.

AUTHOR CONTRIBUTIONS

C.H.: Data curation, Conceptualization, Investigation, Writing-original draft, Formal analysis. Y.Z.: Investigation, Writing-review & editing. E.F.: Investigation, editing. C.D.: Supervision, Conceptualization, Investigation, Formal analysis, Writing-review & editing. X.C.: Visualization, Investigation. X.L.: Supervision, Conceptualization.

COMPETING INTERESTS

The authors declare no competing interests.

ADDITIONAL INFORMATION

Correspondence and requests for materials should be addressed to Cuiwei Du.

Reprints and permission information is available at <http://www.nature.com/reprints>

Publisher's note Springer Nature remains neutral with regard to jurisdictional claims in published maps and institutional affiliations.



Open Access This article is licensed under a Creative Commons Attribution 4.0 International License, which permits use, sharing, adaptation, distribution and reproduction in any medium or format, as long as you give appropriate credit to the original author(s) and the source, provide a link to the Creative Commons license, and indicate if changes were made. The images or other third party material in this article are included in the article's Creative Commons license, unless indicated otherwise in a credit line to the material. If material is not included in the article's Creative Commons license and your intended use is not permitted by statutory regulation or exceeds the permitted use, you will need to obtain permission directly from the copyright holder. To view a copy of this license, visit <http://creativecommons.org/licenses/by/4.0/>.

© The Author(s) 2023